


 Cite this: *RSC Adv.*, 2025, **15**, 30347

Coupled DFT and SCAPS-1D investigation of a novel small-molecule for organic solar cells

Mustafa K. A. Mohammed, ^{*ab} Asmaa Yahya Al-Baitai, ^c Saifaldeen M. Abdalhadi, ^a Vicky Jain, ^d Asha Rajiv, ^e Mayank Kundlas ^f and Helen Merina Albert ^g

Herein, we theoretically developed and studied a novel small-molecule donor, SA1, a phenazine-based derivative, for organic solar cells (OSCs). Density functional theory (DFT) analysis was performed to optimize its electronic and molecular characteristics, which were then employed as input parameters for solar cell capacitance simulator (SCAPS-1D) calculations to explore the photovoltaic properties of the OSC. The SA1 structure incorporated a thieno[3,2-*b*]thiophene bonded with thioxothiazolidin-4-one as an electron-rich part to improve the lowest unoccupied molecular orbital (LUMO) level, while a dibenzo [a,c]phenazine core operated as a weak electron-acceptor part to enhance the highest occupied molecular orbital (HOMO) level. The influences of different layer parameters, such as thickness, doping level, bulk defect density, and density of states, were systematically studied. The effects of fundamental merits, such as electrode work function, parasitic resistances, and temperature, on OSC efficiency were also discussed. After optimization, our OSC device demonstrated a remarkable power conversion efficiency (PCE) of 16.94%, a fill factor (FF) of 87.34%, an open-circuit voltage (V_{OC}) of 1.27 V, and a short-circuit current (J_{SC}) of 15.26 mA cm⁻². Additionally, the designed SA1-based cell showed predictable high thermal stability at 145 °C based on simulation results, along with a high external quantum efficiency (EQE) of 95% in the visible spectrum.

Received 8th July 2025
 Accepted 19th August 2025

DOI: 10.1039/d5ra04889c
rsc.li/rsc-advances

1. Introduction

The global demand for electricity is increasing exponentially, driven by population growth and technological advancement. Fossil fuels, which account for around 80% of the energy supply, are limited in capacity.¹ As a potential alternative to fossil fuels, solar cells have attracted considerable interest in recent decades because of the important issues of global warming, depletion of natural resources, and environmental concerns.^{2,3} Organic solar cells (OSCs) have the potential to play a key role in the future power infrastructure.^{4,5} OSCs have demonstrated rapid progress based on bulk heterojunction or layer-by-layer structures *via* utilizing well-matched polymer

donors and narrow bandgap (E_g) acceptors.^{6,7} In the OSC architecture, the donor and acceptor charge transport materials form a solid-state blend, promoting exciton dissociation at the donor-acceptor interface and enabling simultaneous transfer of holes and electrons to their respective electrodes.⁸ The optimization of interfaces between layers is critical for enhancing charge extraction and minimizing recombination losses in solar cells, as demonstrated in recent studies.^{9–11} It is important to know the energy level requirements for donor molecules, elucidating how suitable energy levels minimize exciton binding energy. Moreover, donor molecules must promote efficient charge transfer with low energy losses.¹² The molecular structure should ideally minimize the electronic coupling coefficient (κ) and energy difference between the HOMO and LUMO (ΔE) to enhance efficacy in light-harvesting or charge transfer. A side chain or peripheral group is necessary to bestow solubility, enabling the processing and fabrication of donor materials into thin films while maintaining fused-ring cores for π -conjugation and rigidity.^{13,14}

Small molecules (SMs) have emerged as competitive alternatives to conjugated polymers in OSCs, owing to their distinct merits, such as well-defined chemical structures, reduced batch-to-batch variation, and easier purification.¹⁵ A class of SMs that has garnered significant attention for use as donor material in OSCs is heterocyclic nitrogen-containing compounds. This class includes versatile compounds with

^aCollege of Remote Sensing and Geophysics, Al-Karkh University of Science, Baghdad 10011, Iraq. E-mail: dr.mustafa@kus.edu.iq

^bCollege of Science, University of Warith Al-Anbiyaa, 56001 Karbala, Iraq

^cChemistry Department, College of Science, Al-Nahrain University, Baghdad 10011, Iraq

^dMarwadi University Research Center, Department of Chemistry, Faculty of Science, Marwadi University, Rajkot, Gujarat, India

^eDepartment of Physics & Electronics, School of Sciences, JAIN (Deemed to be University), Bangalore, Karnataka, India

^fCentre for Research Impact & Outcome, Chitkara University Institute of Engineering and Technology, Chitkara University, Rajpura, 140401, Punjab, India

^gDepartment of Physics, Sathyabama Institute of Science and Technology, Chennai, Tamil Nadu, India



diverse chemical structures, such as phenothiazine,¹⁶ phenoxazine,¹⁷ carbazole,¹⁸ pyrrole,¹⁹ and quinone.²⁰ Among these candidates, phenazine derivative compounds consisting of two fused aromatic rings with one or two nitrogen heteroatoms have been extensively studied in OSCs and other optoelectronic devices.^{21,22} Khanam *et al.* used DFT computation to design non-fullerene SMs containing a phenazine core modified with a variety of substituents at the terminals. The designed molecules showed reduced E_g with enhanced absorptivity.²³ Later, Li and co-workers incorporated a selenium (Se) additive into phenazine-based SMs for OSCs. The synergistic effect of phenazine cores and Se substitution increased light-harvesting capability, resulting in OSC devices with high J_{SC} and a PCE of 17.69%.²⁴ Recently, Wang *et al.* synthesized different SMs based on a phenazine unit with an alkyl chain, π -bridges, and terminal halogenation for OSCs. Three molecules demonstrated near-IR absorption, appropriate energy levels, high stability, and good intermolecular stacking. Consequently, the champion OSCs achieved a performance of 10.11%.²⁵

Extending these developments, our work intends to develop and evaluate a new phenazine-based small molecule for OSCs. A novel phenazine, coded as SA1 (((5Z,5'E)-5,5'-((5,5'-(dibenzo[a,c]phenazine-10,13-diy)bis(thieno[3,2-b]thiophene-5,2-diy))bis(methanlylidene))bis(3-ethyl-2-thioxothiazolidin-4-one))) was designed theoretically by combining a dibenzo[a,c]phenazine unit with thieno[3,2-b]thiophene and thioxothiazolidin-4-one groups in an SM donor. The DFT calculations were utilized to investigate the physical and chemical properties, which were subsequently used as input for SCAPS-1D simulations to predict the photovoltaic performance. The optimized OSC recorded a PCE of 16.94%, a FF of 87.34%, a J_{SC} of 15.26 mA cm⁻², and

a V_{OC} of 1.27 V. The remarkable photovoltaic performance achieved by the SA1-based OSC highlights a novel molecular structure that offers a promising direction for next-generation high-efficiency organic solar cells.

2. Methodology

2.1. Donor designing and computational studies

The SA1 compound was designed as a donor material in OSC, as shown in Fig. 1. The design idea of the SM was represented by using dibenzo[a,c]phenazine as a core in the center of the molecule with two arm molecules of thieno[3,2-b]thiophene and thioxothiazolidin-4-one bonded in the 5,5' position of phenazine. The phenazine core was used due to the distinct advantages, such as enhanced photochemical stability, strong light absorption, and efficient charge transport mobility.²⁶ The thioxothiazolidin-4-one and thieno[3,2-b]thiophene were used as a rich electron part to improve the LUMO, and the phenazine core was used as a weak acceptor part to enhance the HOMO of SA1.²⁷ Gaussian 09W performed all computational studies for SA1. The geometry optimizations and frequency calculations were performed using DFT, followed by TD-DFT calculations to simulate electronic transitions, all using the Becke's three-parameter hybrid function combined with the Lee-Yang-Parr correlation function (B3LYP) functional and 6-311++G** basis set in vacuum. The simulated vibrational frequencies of SA1 have no imaginary peaks, indicating that the simulation has true energy level minima. Fig. 1a shows the electron distribution of HOMO and LUMO for SA1. The electron distribution in HOMO was delocalized in two arms of the compound with energy 5.67 eV, and the electron distribution of LUMO was

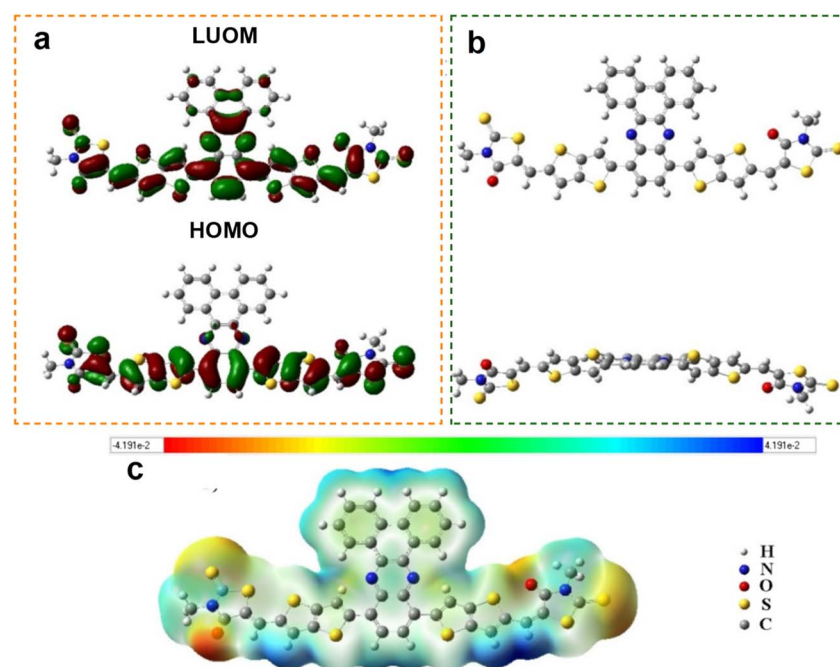


Fig. 1 Description of the designed SA1 organic compound. (a) The electron distribution of the HOMO and LUMO. (b) The optimization structure. (c) The electrostatic potential analysis.



delocalized in the center and arms of the compound with energy 3.82 eV, which gave a good position for the injection of the electron to the LUMO of the acceptor.

Fig. 1b illustrates the optimization structure for SA1. The structure exhibited a moderately planar backbone, as evidenced by DFT-calculated dihedral angles of 32.74° between the core and thieno[3,2-*b*]thiophene. Additionally, the small dihedral angle of 0.21° between the thieno[3,2-*b*]thiophene and terminal unit. This planarity facilitates π - π stacking in the solid state, enhancing intermolecular charge transport.²⁸ Additionally, the extended conjugation from the core through the arm of the

molecule enables efficient electronic delocalization, which contributes to the narrow optical bandgap and strong absorption in the visible region.²⁹ Fig. 1c shows a graphical representation of the electrostatic potential (ESP) generated by a molecule, allowing its charge distribution to be perceived more easily. The high electron cloud in the SA1 was represented in most of the molecule and depicted in green and blue colours. In contrast, a small area of red colours was located in the O atoms of thioxothiazolidin-4-one.³⁰ Generally, the ESP results indicate that the SA1 compound behaves as a nucleophile, particularly in the two benzene rings of the phenazine and the

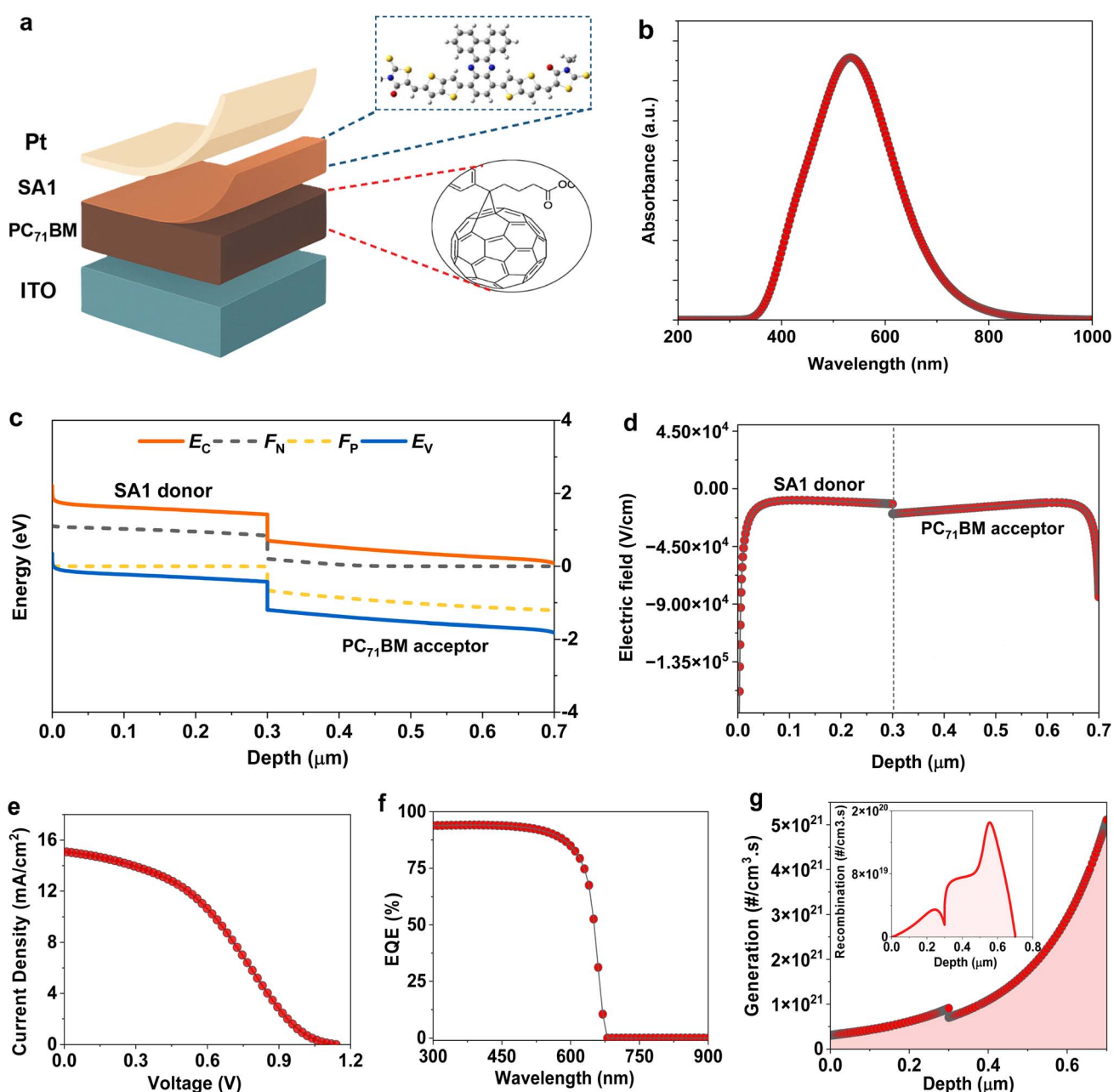


Fig. 2 The architecture and optoelectronic properties of primary planar-heterojunction OSC device. (a) The device structure. (b) Absorption profile of SA1 compound. (c) Energy band diagram. (d) Electric field distribution. (e) The *J*-*V* curve of designed OSC. (f) The corresponding EQE profile. (g) Generation-recombination profile of simulated OSC.



thieno[3,2-*b*]thiophene moiety. The electron-rich (negative potential) regions located on the phenazine core and thieno[3,2-*b*]thiophene units suggest a strong tendency for π - π stacking, which is favorable for efficient hole mobility.

2.2. OSCs device simulation

The SCAPS-1D can be used to calculate energy bands, current-voltage characteristics (*J*-*V*), and the EQE spectrum by solving the Poisson and electron-hole continuity equations. This tool can also determine the distribution of electric fields (*E*) across layers and interlayers, in addition to recombination patterns. The following basic equations for carriers are used in this software:^{31,32}

$$\frac{d}{dx} \left(-\varepsilon(x) \frac{d\varphi}{dx} \right) = q[p(x) - n(x) + N_D^+(x) - N_A^-(x) + p_t(x) + n_t(x)] \quad (1)$$

$$\frac{dJ_n}{dx} = G - R \quad (2)$$

$$\frac{dJ_p}{dx} = G - R \quad (3)$$

The charge carrier transport processes can be explained by the drift-diffusion approach:

$$J_n = qD_n \frac{dn}{dx} + q\mu_n n \frac{d\varphi}{dx} \quad (4)$$

$$J_p = qD_p \frac{dp}{dx} + q\mu_p p \frac{d\varphi}{dx} \quad (5)$$

where $\varepsilon(x)$: the position-dependent permittivity of the material, ψ : electrostatic potential, q : elementary charge, $n(x)$ and $p(x)$ are density of free electrons and holes, respectively. N_D^+ and N_A^- are ionized donor and acceptor dopant concentrations. $n_t(x)$ and $p_t(x)$ are the density of trapped electrons and holes, respectively, R : recombination rate of carriers, G : generation rate of carriers, J_n : electron current density, J_p : hole current density, D_n :

diffusion coefficient for electron, D_p : diffusion coefficient for hole, μ_n : electron mobility, μ_p : hole mobility.

All calculations are conducted at an atmospheric temperature of 300 K under the AM1.5 solar spectrum and a frequency of 1 MHz. Furthermore, the values of $2 \Omega \text{ cm}^2$ for series resistance (R_s) and $10^4 \Omega \text{ cm}^2$ for shunt resistance (R_{shunt}) were inserted to simulate OSC devices. These values are consistent with optimized device conditions reported in literature and reflect efficient charge extraction and minimal leakage current. The designed SA1 compound with an ionization energy (IP) of 5.6 eV is used as a novel electron donor material. A typical [6,6]-phenyl-C71-butyric acid methyl ester (PC₇₁BM) is utilized as an acceptor layer. The OSC components demonstrated in Fig. 2a were employed in the development of the model, including an indium tin oxide (ITO) and platinum (Pt) metal as front and back electrodes, respectively. The work function values of the ITO and Pt contacts were assigned to be 4 eV and 5.4 eV, respectively.^{33,34} Tables 1 and 2 display the essential characteristics of the primary OSC (ITO/PC₇₁BM/SA1/Pt) obtained by integrating the available experimental and theoretical results.³⁵⁻⁴¹ The defect density at the SA1/PC₇₁BM interface was 10^{11} cm^{-2} , while the carrier charge's thermal velocity (V_{th}) was maintained at 10^7 cm s^{-1} . As shown in Fig. 2b, the ultraviolet-visible (UV-vis) spectrum of SA1 has a broad absorption range from 350 nm to 750 nm, with a pronounced peak close to 600 nm, indicating that SA1 could effectively absorb photons in the visible range. This high absorption in the visible region is further supported by the EQE of the OSC device (Fig. 2f). The

Table 2 Interface properties of ITO/PC₇₁BM/SA1/Pt planar OSCs

Parameters/interfaces	SA1/PC ₇₁ BM
Type of defect	Neutral
Cross-section for electron capture (cm^2)	1.0×10^{-19}
Cross-section for hole capture (cm^2)	1.0×10^{-19}
Distribution of energies	Single
Reference for energy level of defect (E_t)	Above the highest E_v
Energy measured with respect to reference (eV)	0.600
Defect density (cm^{-2})	1.0×10^{11}

Table 1 Description of parameters utilized in the planar heterojunction OSCs

Parameters	SA1	PC ₇₁ BM	Y6-4O	ITIC-4F	o-BTP-eC9
Thickness (nm)	300	400	500	500	500
E_g (eV)	1.848	1.9	1.63	1.71	1.84
χ_e (eV)	3.2	3.92	4.01	4.02	3.86
HOMO (eV)	-5.677	-6.1	-5.64	-5.73	-5.70
LUMO (eV)	-3.829	-4.2	-4.01	-4.02	-3.86
ε_r	8	6	5.13	3.94	2.9
N_C (cm^{-3})	1.0×10^{20}	1.0×10^{19}	1.0×10^{19}	1.0×10^{19}	1.0×10^{19}
N_V (cm^{-3})	1.0×10^{19}	1.0×10^{20}	1.0×10^{20}	1.0×10^{20}	1.0×10^{20}
μ_e ($\text{cm}^2 \text{ V}^{-1} \text{ s}^{-1}$)	5×10^{-2}	1×10^{-2}	0.92×10^{-4}	2.93×10^{-4}	3.5×10^{-4}
μ_h ($\text{cm}^2 \text{ V}^{-1} \text{ s}^{-1}$)	5×10^{-2}	1×10^{-2}	0.92×10^{-4}	2.93×10^{-4}	4×10^{-4}
N_D (cm^{-3})	1.0×10^{15}	—	—	—	—
N_A (cm^{-3})	—	1.0×10^{18}	1.0×10^{18}	1.0×10^{18}	1.0×10^{18}
N_T (cm^{-3})	1.0×10^{15}	1.0×10^{14}	1.0×10^{14}	1.0×10^{14}	1.0×10^{14}



absorption is ascribed to $\pi-\pi$ electronic transitions enabled by the extensive coupling of the dibenzo[*a,c*]phenazine and thieno[3,2-*b*]thiophene moieties.

Fig. 2c displays the energy band diagram after contact. The energy level scheme indicates properly matched energy levels

that promote effective carrier separation and transportation. The conduction band and valence band demonstrate band bending, facilitating the formation of a built-in potential (V_{bi}) at the interface, which promotes exciton dissociation and decreases the recombination rate (Fig. 2d). The obtained $J-V$

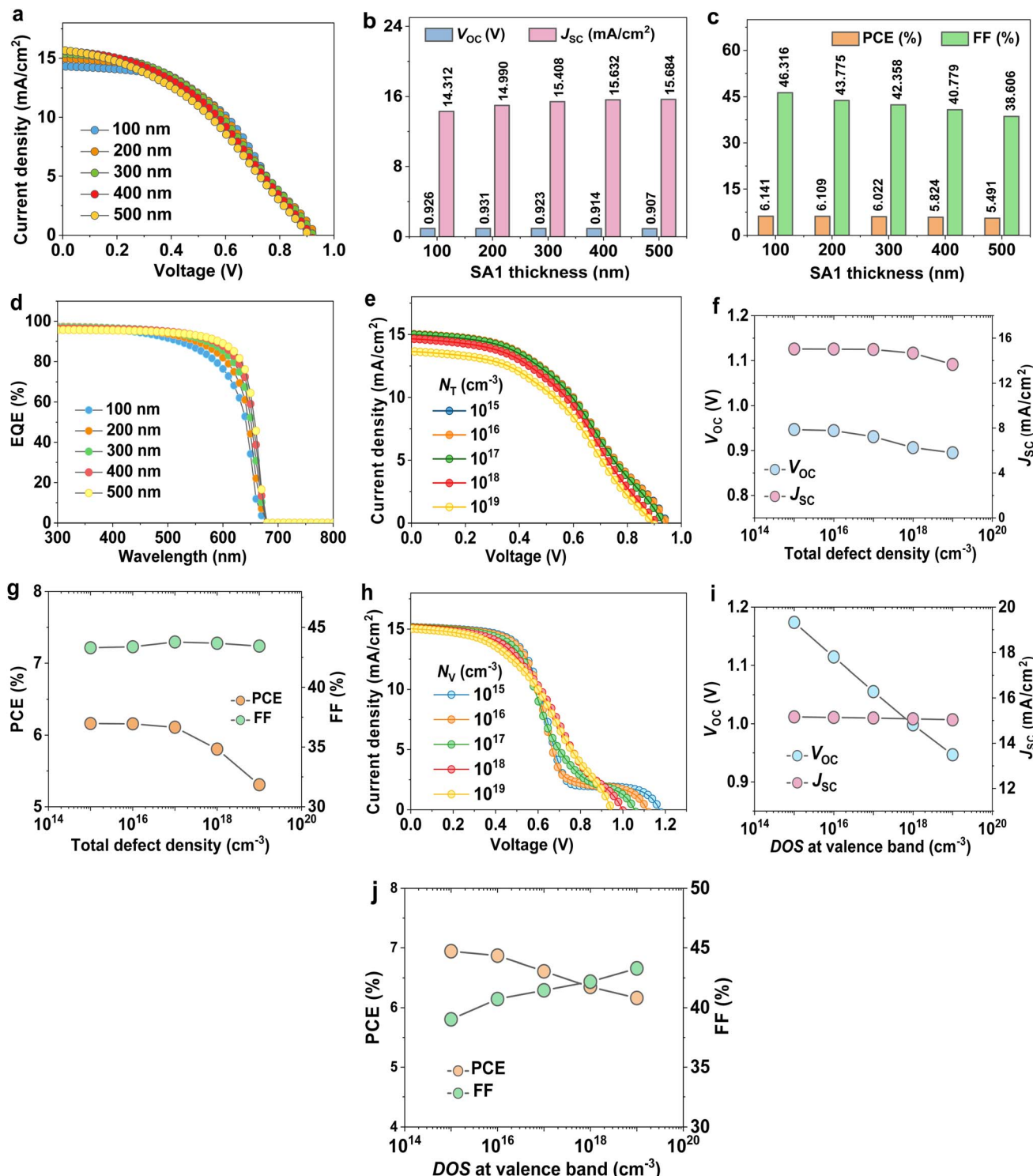


Fig. 3 Optimization of the designed SA1 organic compound. (a) $J-V$ curves of cells at various thicknesses. The related cell parameters: (b) V_{oc} , J_{sc} , (c) FF, PCE, and (d) EQE. (e) The variation defect density on $J-V$ plots. Variation in (f) V_{oc} , J_{sc} , (g) FF, and PCE. (h) $J-V$ plots variation with DOS at the valence band. Related parameters are (i) V_{oc} , J_{sc} , (j) FF, and PCE.



photovoltaic characteristic of the primary OSC is shown in Fig. 2e. From our initial calculations, the designed OSC revealed an efficiency of 6.02%, a FF of 35.23%, a V_{OC} of 1.109 V, and a J_{SC} of $15.408 \text{ mA cm}^{-2}$. Additionally, the EQE of the designed OSC is exhibited in Fig. 2f. The SA1 material in this OSC device

exhibits efficient light-harvesting capability within the wavelength range of 300–600 nm. Fig. 2g illustrates that a significant generation rate is attained for the OSC device, which correlates with elevated J_{SC} and PCE values.

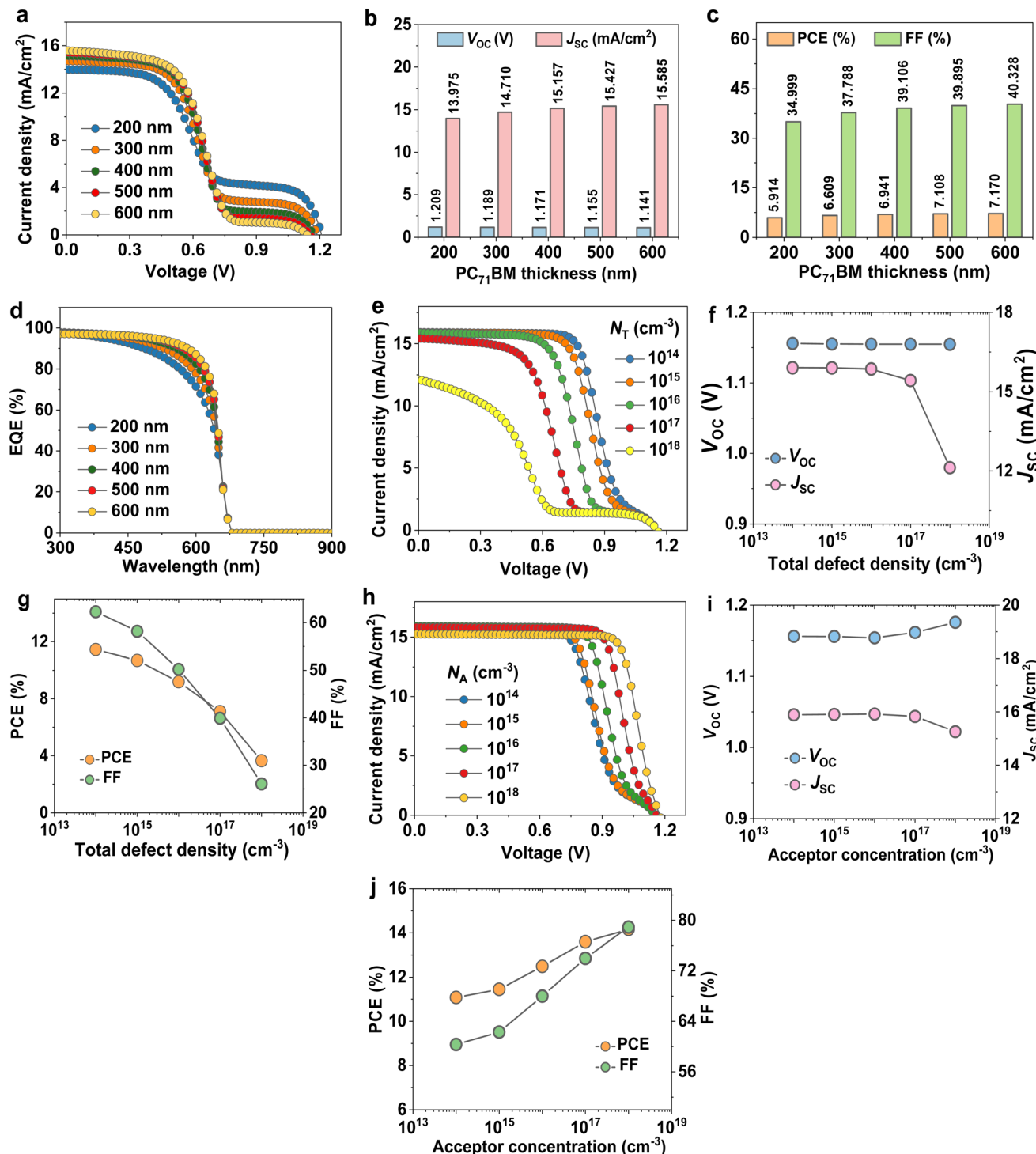


Fig. 4 Optimization of the PC₇₁BM acceptor compound. (a) J – V profiles of OSCs with different thicknesses. The related cell parameters: (b) V_{OC} , J_{SC} , (c) FF, PCE, and (d) EQE. (e) The variation bulk defect density on J – V plots. Variation in (f) V_{OC} , J_{SC} , (g) FF, and PCE. (h) J – V curves at different shallow acceptor concentration (N_A). Corresponding parameters are (i) V_{OC} , J_{SC} , (j) FF, and PCE.



3. Results and discussion

To optimize the DFT-designed SA1 compound, we probe the impact of SA1 thickness variation on photovoltaic parameters. At first, it is obvious from Fig. 3a that SA1-based OSC is recording the optimal performance at 200 nm, $V_{OC} = 0.931$ V, $J_{SC} = 14.99$ mA cm $^{-2}$, FF = 43.775%, and PCE = 6.109%. As shown in Fig. 3b, the J_{SC} demonstrated a marginal improvement with increased SA1 thickness and eventually reached a saturation point at a 400 nm-thick layer. The improvement in J_{SC} can originate from improved absorption of long-wavelength photons, which raises the generation of electron-hole pairs. In cases where the photoactive thickness is low, only a limited number of long-wavelength photons are captured, resulting in a low production of carriers and, consequently, a reduced J_{SC} .⁴² These results are consistent with the EQE spectral response (Fig. 3d). The highest EQE response of the OSC based on SA1 was reached at 400–500 nm. Generally, the FF of OSCs reduces with the increase of absorber thickness (see Fig. 3c). The FF of OSCs is reduced severely from 46.316% to 38.606% when the thickness increases from 100 nm to 500 nm.⁴³ Actually, due to their short lifetime and prominent low exciton diffusion length (L), traditional OSC optimum performance is usually attained with a relatively thin photoactive layer, not more than 150 nm.⁴⁴

The total defect density (N_T) value in the SA1 active film changed within the range of 10^{15} to 10^{19} cm $^{-3}$ to investigate the most favorable defect density for the designed OSCs. Fig. 3e–g illustrate the relationship between the N_T variation and the OSC

output parameters, implying a notable reduction in PCE and V_{OC} as the N_T increases. The increase in recombination rate reduces the L value, thereby decreasing the efficiency. Prajapati and co-workers have adopted a similar effect.⁴⁵ The desirable N_T , achieving a PCE of around 6.109% for this specific cell, was determined to be 10^{16} cm $^{-3}$.

Fig. 3h shows J – V characteristic curves of OSCs with various densities of states at the valence band (N_V) of the SA1 compound. The V_{OC} can be given by:

$$V_{OC} = \frac{KT}{q} \ln\left(\frac{J_{SC}}{J_0} + 1\right) \quad (6)$$

where J_0 is the reverse saturation current density given by:

$$J_0 = qN_C N_V e^{-\frac{E_g}{KT}} \quad (7)$$

when N_V increases, J_0 also increases, leading to a lower V_{OC} , as depicted in Fig. 3i. A higher N_V indicates that more available states in the valence band lead to increased recombination processes, further suppressing V_{OC} . Since efficiency is directly related to V_{OC} , a decline in V_{OC} decreases the overall performance (see Fig. 3j).

To further improve the photovoltaic properties of SA1-based OSC, the PC₇₁BM acceptor layer was optimized. Regarding the optimization process, the thickness of the PC₇₁BM film is altered to investigate the influence of its variation on the device performance. The thickness of PC₇₁BM is changed from 200 nm to 600 nm, as shown in Fig. 4a. As the thickness increases, the J_{SC} increases, as depicted in Fig. 4b, due to increasing light

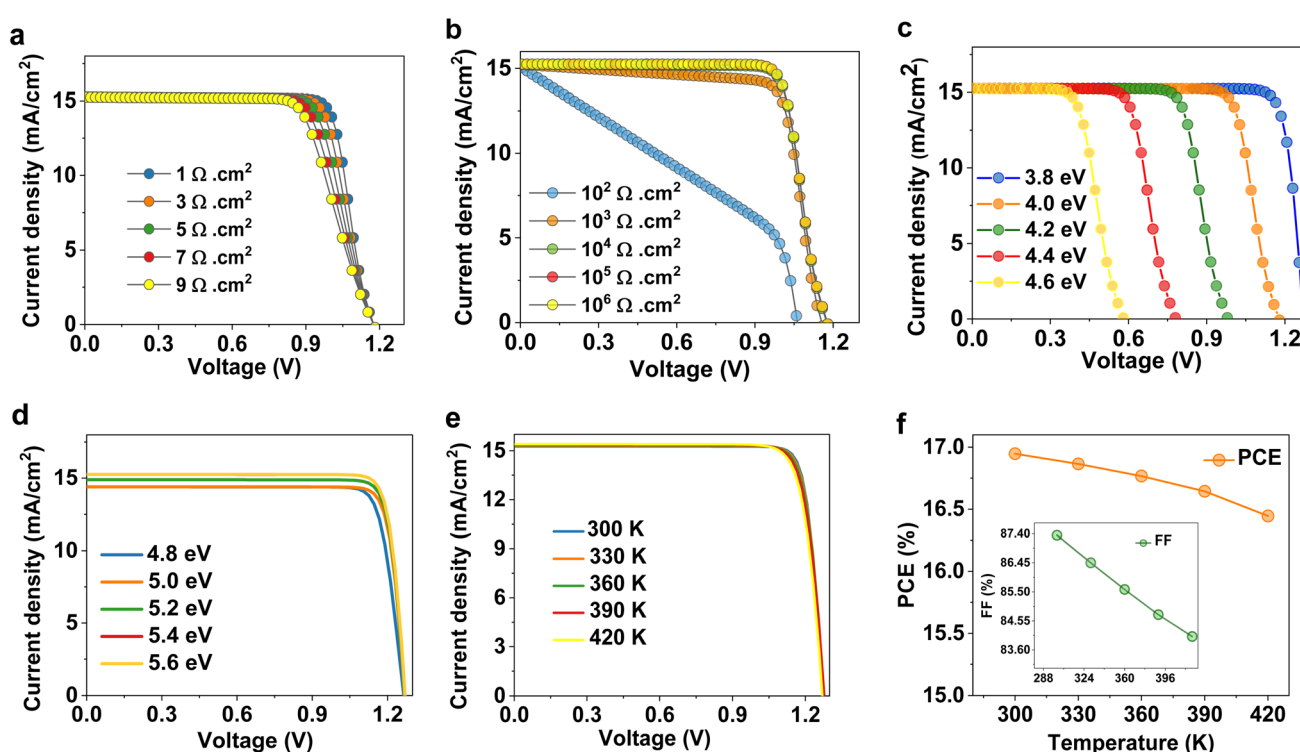


Fig. 5 Optimization of parasitic resistances, electrodes, and operational temperature. (a) J – V plots of OSCs at different R_S . (b) J – V plots of OSCs at different R_{Shunt} . (c) J – V characteristics of OSCs at different work functions of front electrode. (d) J – V profiles of cells at different work functions of back electrode. (e) J – V curves and (f) device parameters at different temperatures.



absorption and photo-induced electron–hole pairs. As shown in Fig. 4c, the PC₇₁BM thickness of 500 nm was chosen as it provides an optimized PCE by balancing efficiency and voltage.⁴⁶ Additionally, a remarkable enhancement in FF was shown with increasing PC₇₁BM thickness, which is related to suppressing R_s and improving charge transportation. The optimized PC₇₁BM film promotes effective electron collection while mitigating recombination losses at the donor–acceptor interface (see Fig. 4d).

Furthermore, we explore the impact of the variation of bulk trap density on the photovoltaic merits of OSC devices. The calculation findings of the variation of the defect states from 10^{14} cm^{-3} to 10^{18} cm^{-3} on the J – V plot are demonstrated in Fig. 4e. As can be noticed from Fig. 4f and g, PC₇₁BM defect density has a significant effect on the functionality of the OSCs. As defect concentration increases, decomposition in device parameters occurs because of increasing traps and recombination sites. Increasing defects leads to a reduction in the charge lifetime, and thus the recombination process increases. At 10^{14} cm^{-3} defect concentration, the OSC device achieved optimum performance with a V_{OC} of 1.155 V, a J_{SC} of $15.904 \text{ mA cm}^{-2}$, a FF of 62.297%, and a PCE of 11.452%.

Dopant attempts to facilitate effective charge transfer, hence enhancing conductivity and balancing energy bands with the electrodes and the absorber interface, which results in increased efficiency. To characterize doping influence on device parameters, we changed the acceptor doping concentration (N_A) of PC₇₁BM from 10^{14} cm^{-3} to 10^{18} cm^{-3} (Fig. 4h). As depicted in Fig. 4i, a slight reduction in J_{SC} value was observed beyond the 10^{17} cm^{-3} doping level. Therefore, optimizing the doping concentration within the moderate range can help maintain efficient charge extraction and minimize recombination losses. As the N_A increased, a remarkable enhancement in FF and efficiency was recorded due to the V_{bi} effect.⁴⁷ This improvement in the V_{bi} improves the extraction of carriers, giving rise to FF, as shown in Fig. 4j. Considering all these factors, the best magnitude for the N_A of PC₇₁BM was selected to be 10^{18} cm^{-3} . The device outputs at this concentration are PCE = 14.157%, FF = 78.916%, V_{OC} = 1.175 V, and J_{SC} = $15.257 \text{ mA cm}^{-2}$.

The influence of R_s on the photovoltaic efficiency of the OSC was thoroughly analyzed by altering R_s from $1 \Omega \text{ cm}^2$ to $9 \Omega \text{ cm}^2$, as shown in Fig. 5a. The findings indicated a notable reduction in FF and PCE, although V_{OC} and J_{SC} remained unchanged

(Table 3). This tendency is ascribed to increased ohmic losses, which impede carrier collection and induce extra voltage drops within the cell, hence diminishing the maximum energy output.⁴⁸ The reduction in FF immediately affects PCE, emphasizing the necessity of reducing R_s for effective carrier transfer. We simulated R_{Shunt} values between $10^2 \Omega \text{ cm}^2$ and $10^6 \Omega \text{ cm}^2$ to investigate how OSC efficiency is affected. Fig. 5b displays the J – V profiles varying with R_{Shunt} . With rising R_{Shunt} , the V_{OC} , FF, and PCE all progressively improve; the J_{SC} stays constant. The R_{Shunt} value was raised, and the efficiency improved from 5.76% to 14.46%. The V_{OC} decreases severely at low R_{Shunt} due to increased leakage currents, while it remains nearly constant at higher R_{Shunt} values where leakage becomes negligible.⁴⁹ Our calculation indicates that an efficiency of 14.46% can be obtained with an R_{Shunt} of $10^5 \Omega \text{ cm}^2$ (Table 3).

Fig. 5c reveals the variations in the metal work function of the right contact from 3.8 eV to 4.6 eV in relation to the photovoltaic outputs of the cells. As illustrated in Table 4, while the J_{SC} was comparable, the V_{OC} , FF, and PCE showed a substantial drop. This decrease is caused by an increase in the carrier transporting barrier at the interface between the electrode and PC₇₁BM, which in turn causes higher charge aggregation and recombination losses as a result of energy band misalignment.⁵⁰

The back Pt metal operates as the hole-collecting electrode, requiring its work function to be compatible with the HOMO of the SA1 layer. The energy barrier of 4.8 eV between the HOMO of

Table 4 The variation of key parameters of OSCs with front and back work functions

Work function of electrode (eV)	V_{OC} (V)	J_{SC} (mA cm^{-2})	FF (%)	PCE (%)
Front electrode	3.8	1.271	15.261	87.347
	4.0	1.178	15.260	80.477
	4.2	0.981	15.259	76.879
	4.4	0.781	15.258	71.987
	4.6	0.581	15.256	64.265
Back electrode	4.8	1.264	14.399	85.570
	5.0	1.269	14.403	87.430
	5.2	1.270	14.894	87.386
	5.4	1.271	15.261	87.347
	5.6	1.271	15.262	87.347
				16.947
				14.469
				11.514
				8.583
				5.701
				15.586
				15.980
				16.534
				16.947
				16.948

Table 3 The variation of key parameters of OSCs with R_s and R_{Shunt}

Resistance		V_{OC} (V)	J_{SC} (mA cm^{-2})	FF (%)	PCE (%)
Series resistance ($\Omega \text{ cm}^2$)	1	1.175	15.259	80.123	14.375
	3	1.175	15.255	77.724	13.942
	5	1.175	15.252	75.333	13.510
	7	1.175	15.249	72.951	13.080
	9	1.175	15.246	70.576	12.652
Shunt resistance ($\Omega \text{ cm}^2$)	10^2	1.063	15.109	35.856	5.760
	10^3	1.155	15.245	76.733	13.522
	10^4	1.175	15.259	80.123	14.375
	10^5	1.177	15.260	80.445	14.461
	10^6	1.178	15.260	80.477	14.469



SA1 and Pt is considerable, resulting in diminished hole injection and charge accumulating at the interface (Fig. 5d). As the work function rises to 5.4 eV, the band matching enhances, leading to less interfacial charge accumulation and minimized recombination rates. This results in a marginal enhancement in J_{SC} as an increased number of photocarriers participate in the photocurrent. The optimized SA1-based OSC recorded a PCE of 16.94% at front and back work functions of 3.8 eV and 5.4 eV, respectively. The SA1-based OSC device achieved a high FF of 87.34%, reflecting effective charge-carrier transport and reduced recombination rates under the simulated conditions. However, the overall efficiency (16.94%) remains moderate due to limitations in photocurrent generation (15.26 mA cm^{-2}), which are governed by the intrinsic absorption range of OSC.

The operational temperature of a solar cell influences its efficiency. Increasing the ambient temperature adversely affects the charge carrier mobility, resulting in reduced device performance.⁵¹ The operating temperature is assessed to be 300–420 K, and the measuring parameters are depicted in Fig. 5e and f.

Figures indicate that the increment in temperature leads to a slight reduction in the V_{OC} . The V_{OC} decline due to higher temperature leads to a shrinkage in the E_g of the light-harvesting material.⁵² Meanwhile, the J_{SC} parameter is unchanged due to increasing temperatures. Additionally, increasing temperatures induce more lattice vibrations, diminishing photo-induced carrier mobility because of intensified phonon scattering, which subsequently elevates R_S and decreases the FF. Higher thermal energy also promotes recombination rates, mainly SRH and Auger recombination processes, further restricting charge collection. Overall, there is a slight decrease in PCE from 16.94% to 16.06%. Thus, the simulated OSC with the SA1 compound is highly stable at higher temperatures.

To evaluate the versatility and practical applicability of the newly designed SM donor SA1, we simulated its combination with four different acceptors: the traditional fullerene-based PC₇₁BM and three state-of-the-art non-fullerene acceptors (NFAs)—Y6, ITIC-4F, and BTP-eC9. As shown in Fig. 6a, all OSCs

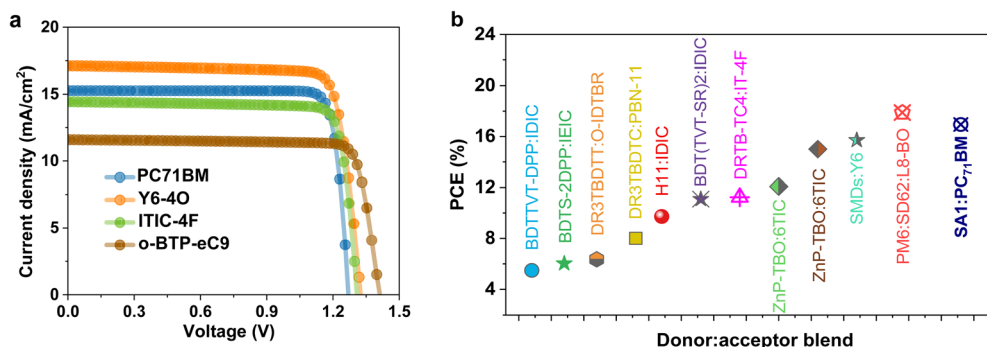


Fig. 6 The final optimized SA1-based OSC and comparison with different non-fullerene acceptor devices. (a) J – V characteristics of simulated OSCs based on different acceptors. (b) Comparison of SA1-OSC with literature-reported SM donors.

Table 5 Description of photovoltaic characteristics of reported small molecule-based organic solar cells^a

Author	Structure	V_{OC} (V)	J_{SC} (mA cm^{-2})	FF (%)	PCE (%)	Stability
Huo <i>et al.</i> ⁵³	ITO/PEDOT:PSS/BDTTVT-DPP:IDIC/PDIN/Al	0.82	11.30	59.17	5.48	Not reported
Lin <i>et al.</i> ⁵⁴	ITO/ZnO/BDTS-2DPP:IEIC/MoO _x /Ag	0.94	10.87	59.00	6.03	Not reported
Yang <i>et al.</i> ⁵⁵	ITO/PEDOT:PSS/DR3TBDTT:O-IDTBR/BCP/Al	1.15	11.06	50.00	6.36	Not reported
Zhang <i>et al.</i> ⁵⁶	TO/ZnO/DR3TBDTC:PBN-11/MoO ₃ /Al	1.11	11.18	64.60	8.01	Retain 89% after 168 hours at 180 °C and 74% after 72 hours under illumination
Bin <i>et al.</i> ⁵⁷	ITO/PEDOT:PSS/H11:IDIC/PDINO/Al	0.97	15.21	65.46	9.73	Not reported
Guo <i>et al.</i> ⁵⁸	ITO/PEDOT:PSS/BDT(TVT-SR) ₂ :IDIC/PDINO/Al	0.98	15.92	71.15	11.10	Retain 49% after 96 hours at 80 °C and 90% after 200 hours under illumination
Yang <i>et al.</i> ⁵⁹	ITO/ZnO/DRTB-TC4:IT-4F/MoO ₃ /Al	0.91	18.27	68.00	11.24	Not reported
Gao <i>et al.</i> ⁶⁰	ITO/PEDOT:PSS/ZnP-TBO:6TIC/C ₆₀ -bissalt/Ag	0.80	20.44	73.87	12.08	Retain 97% after 100 hours in air (25 °C, humidity <15%)
Gao <i>et al.</i> ⁶¹	ITO/PEDOT:PSS/SMD:BO-4Cl/PFN-Br:MA/Ag	0.84	24.38	72.7	15.00	Retain 70% after 450 hours at 80 °C
Guo <i>et al.</i> ⁶²	ITO/PEDOT:PSS/SMDs:Y6/PDINN/Ag	0.84	26.64	69.70	15.71	Retain 75% after 225 hours under illumination
Wang <i>et al.</i> ⁶³	ITO/PEDOT:PSS/PM6:SD62:L8-BO/PNDIT F3N/Ag	0.88	26.08	77.75	17.88	Retain 75% after 250 hours under illumination
This work	ITO/SA1/PC₇₁BM/Pt	1.27	15.26	87.34	16.94	Retain 94% at 145 °C

^a PEDOT-PSS: poly(3,4-ethylenedioxythiophene)-poly-(styrene-sulfonate); PDINO: perylene diimide functionalized with amino N-oxide.



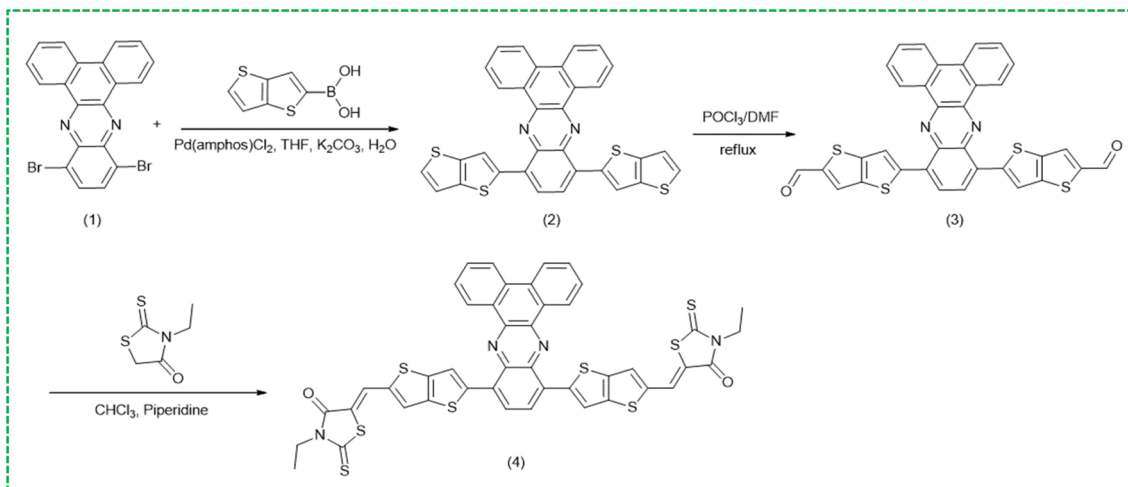


Fig. 7 The synthetic pathway suggestion of SA1 compound.

share an identical architecture, differing only in the acceptor layer, which enables a direct assessment of the acceptor's influence on device performance. Notably, the SA1:Y6-4O cell showed the best-performing PCE, driven by high J_{SC} and FF. This pattern can be attributed to Y6-4O's broad absorption spectrum extending into the near-infrared region, its favorable energy level alignment with SA1, and its high dielectric constant, which together facilitate effective exciton dissociation and charge carrier collection. The cells based on ITIC-4F and o-BTP-eC9 showed high photovoltaic performance, with efficiencies that closely rival that of Y6-4O. Table 5 and Fig. 6b summarize a comparison of our proposed SA1-based OSC with existing reported SM donor structures. With an ITO/SA1/PC₇₁BM/Pt pattern, the cell developed in this study had a significantly high PCE of 16.94% and a FF of 87.34%, exceeding several previously published SM-based OSCs. Regarding thermal stability, our device maintained 94% of its starting efficiency under 145 °C, surpassing previous systems displaying performance loss under comparable or less harsh environments.

Finally, to ensure the designed SA1 compound is not only theoretically promising but also synthetically viable, a three-step synthetic route is suggested, inspired by established organic methodologies commonly applied in the synthesis of π -conjugated donor materials. The synthesis of SA1 could involve three reaction steps (Fig. 7). First, a Suzuki–Miyaura coupling reaction occurs between 10,13-dibromodibenzo[a,c]phenazine (1) and thieno[3,2-b]thiophen-2-ylboronic acid, leading to the formation of compound (2). Next, compound (3) is synthesized *via* the Vilsmeier–Haack reaction. Lastly, the resulting compound undergoes a Knoevenagel condensation reaction to yield SA1.

4. Conclusion

In summary, a novel phenazine-based SM compound, SA1, was computationally designed for planar-heterojunction OSCs. We explored the potential of SA as the electron donor layer in SM-

based OSCs. The developed ITO/PC₇₁BM/SA1/Pt architecture was systematically optimized for thickness, bulk defect states, doping level, and effective density of states concentration using SCAPS-1D numerical software. The findings indicate that the preferred thicknesses of SA1 and PC₇₁BM are 200 nm and 500 nm, respectively. Besides, optimizing the PC₇₁BM doping level to 10^{18} cm^{-3} was determined to be beneficial for increasing the simulated OSC's performance. Similarly, the optimal defect levels are measured as 10^{16} cm^{-3} , and 10^{14} cm^{-3} for the SA1 and PC₇₁BM, respectively. Our results reveal that by suppressing R_S and increasing R_{Shunt} , the cell performance can be improved. The optimized OSC device showed remarkable performance, obtaining a PCE of 16.94%, FF of 87.34%, a V_{OC} of 1.27 V, a J_{SC} of 15.26 mA cm^{-2} , and an EQE of 95%. The temperature dependencies of photovoltaic parameters were examined across the range of 300 K to 420 K to assess heating stressors. Interestingly, the designed OSC structure showed stable behavior over this temperature range, suggesting good predicted thermal tolerance. The comparison of PC₇₁BM-based OSCs with three different NFAs (Y6-4O, ITIC-4F, and o-BTP-eC9) exhibited that the acceptor layer influences device performance. Among them, the SA1:Y6-4O device showed the most promising photovoltaic parameters, highlighting the synergy between the designed donor and state-of-the-art acceptors.

Conflicts of interest

The authors declare no conflict of interest.

Data availability

The data will be available from the corresponding author on reasonable request.

Acknowledgements

We would like to express our sincere gratitude to Marc Burgelman and his team at the University of Gent, Belgium, for

developing the SCAPS-1D simulation tool, which has been instrumental in the progress of this research.

References

- 1 F. L. Rashid, A. Hashim, A. Dulaimi, A. Hadi, H. Ibrahim, M. A. Al-Obaidi and A. Ameen, Enhancement of Polyacrylic acid/Silicon carbide Nanocomposites' optical properties for potential application in renewable energy, *J. Compos. Sci.*, 2024, **8**(4), 123.
- 2 H. Togun, A. Basem, A. A. H. Kadhum, A. M. Abed, N. Biswas, F. L. Rashid, R. A. Lawag, H. M. Ali, H. I. Mohammed and D. K. Mandal, Advancing photovoltaic thermal (PV/T) systems: innovative cooling technique, thermal management, and future prospects, *Sol. Energy*, 2025, **291**, 113402.
- 3 A. Basem, S. Opakhai, Z. M. S. Elbarbary, F. Atamurotov and N. E. Benti, A comprehensive analysis of advanced solar panel productivity and efficiency through numerical models and emotional neural networks, *Sci. Rep.*, 2025, **15**(1), 259.
- 4 H. Togun, A. Basem, M. J. Jweeg, N. Biswas, A. M. Abed, D. Paul, H. I. Mohammed, A. Chattopadhyay, B. K. Sharma and T. Abdulrazzaq, Advancing organic photovoltaic cells for a sustainable future: the role of artificial intelligence (AI) and deep learning (DL) in enhancing performance and innovation, *Sol. Energy*, 2025, **291**, 113378.
- 5 W. Xu, H. Zhou, H. Tian, L. Zhang, J. Du, J. Yao, S. Y. Jeong, H. Y. Woo, E. Zhou and X. Ma, Achieving light utilization efficiency of 3.88% and efficiency of 14.04% for semitransparent layer-by-layer organic solar cells by diluting donor layer, *Chem. Eng. J.*, 2025, **508**, 161148.
- 6 H. Zhou, L. Zhang, H. Tian, Y. Ni, Y. Xie, S. Y. Jeong, T. Huang, H. Y. Woo, J. Zhang and X. Zhu, Layered All-Polymer Solar Cells with Efficiency of 18.34% by Employing Alloyed Polymer Donors, *Small*, 2025, **21**(11), 2410581.
- 7 H. Tian, W. Xu, Z. Liu, Y. Xie, W. Zhang, Y. Xu, S. Y. Jeong, F. Zhang, N. Weng and Z. Zhang, Over 18.8% efficiency of layer-by-layer organic photovoltaics enabled by ameliorating exciton utilization in acceptor layer, *Adv. Funct. Mater.*, 2024, **34**(16), 2313751.
- 8 W. Miao, Y. Liu, Y. Wu, J. Liang, J. Xiong, T. Hu, Y. He, L. Chen, J. Shan and X. Wang, Energy Disorder Suppression, Charge Transport Channel Establishment by Integrating Four-Arm Donor Molecule for High-Performance Organic Solar Cells, *Adv. Funct. Mater.*, 2025, 2501143.
- 9 Y. Yang, S. Chen, Z. Dai, H. Wei, S. Wan, Y. Chen, J. Sun, Z. Liu, L. Ding and H. Xia, Bridged Carbolong Modulating Interfacial Charge Transfer Enhancement for High-Performance Inverted Perovskite Solar Cells, *Angew. Chem.*, 2025, **137**(8), e202420262.
- 10 Y. Yang, S. Wan, H. Wei, L. Yang, Z. Dai, H. Lu, Z. Liu, B. Chen, R. Chen and H. Wang, Sustainable protection of natural liquid enables ultra-stable inverted perovskite solar cells via allylic disulfide rearrangement, *Energy Environ. Sci.*, 2025, **18**(10), 4962–4970.
- 11 X. Xiao, Z. Dai, Y. Yang, L. Yuan, S. Wan, Y. Yang, T. He, Z. Hu, X. He and F. Li, Surface Chemical Conversion of Residual PbI₂ Enables Efficient and Stable Perovskite Solar Cells by 1, 3-Diphenyl-benzimidazolium Iodide Treatment, *Adv. Funct. Mater.*, 2025, 2418792.
- 12 A. Y. Al-Baitai, M. Mahmood, S. F. Abdulhussein and S. M. Abdalhadi, Metals doped TiO₂ nanoparticle as an efficient photoelectrode in dye-sensitized solar cells: a review, *Nanochem. Res.*, 2024, **9**(3), 207–215.
- 13 T. Zhao, X. Jin, M.-H. Li, J. Li, S. Wang, Z. Zhang, P. Sun, S. Lin, Q. Chen and J.-S. Hu, π -Conjugation-Induced In Situ Nanoscale Ordering of Spiro-OMeTAD Boosts the Efficiency and Stability of Perovskite Solar Cells, *J. Am. Chem. Soc.*, 2024, **146**(45), 30893–30900.
- 14 S. Singh, S. Kumar, D. B. Pal and R. Ganguly, Porous Organic Polymers for Renewable Energy Development, Renewable Energy Development: Technology, *Mater. Sustain.*, 2025, 241–259.
- 15 H. Chen, Y. Huang, R. Zhang, H. Mou, J. Ding, J. Zhou, Z. Wang, H. Li, W. Chen and J. Zhu, Organic solar cells with 20.82% efficiency and high tolerance of active layer thickness through crystallization sequence manipulation, *Nat. Mater.*, 2025, 1–10.
- 16 W. Taouali, A. Azazi, R. Hassani, E. H. El-Araby and K. Alimi, Exploring the Impact of Structural Modifications of Phenothiazine-Based Novel Compounds for Organic Solar Cells: DFT Investigations, *Polymers*, 2025, **17**(1), 115.
- 17 T. Hu, C. Yu, R. Luo, X. Zhao, R. Yu, J. Wu, Y. Huo and N. Cai, Alkyl Fluoride Modification-Enhanced Intermolecular Interactions of Phenoxazine-Based Hole-Transporting Materials for Efficient and Stable Inverted Perovskite Solar Cells, *Sol. RRL*, 2025, **9**, 2400795.
- 18 C. Liu, Y. Lian, J. Song, J. Liu, Z. Bi, W. Ma and Y. Sun, Oligomeric Carbazole Phosphonic Acid as Hole-Transporting Layer for Organic Solar Cells With Efficiency of 19.63%, *Adv. Funct. Mater.*, 2025, 2417786.
- 19 B.-W. Chen, M.-W. An, K. Wang, S. Y. Jeong, X. Wang, Z.-L. Qiu, K. Cao, S.-Y. Zheng, L. Wang and H. Y. Woo, Unprecedented short-circuit current density and efficiency of vacuum-deposited organic solar cells based on 8H-thieno [2', 3': 4, 5] thieno [3, 2-b] thieno [2, 3-d] pyrrole, *Sci. Bull.*, 2025, **70**, 897–904.
- 20 C. Guo, Y. Sun, L. Wang, C. Liu, C. Chen, J. Cheng, W. Xia, Z. Gan, J. Zhou and Z. Chen, Light-induced quinone conformation of polymer donors toward 19.9% efficiency organic solar cells, *Energy Environ. Sci.*, 2024, **17**(7), 2492–2499.
- 21 S. Jahanbani and R. Ghadari, Investigating the Effect of Nitrogen and Chlorine co-Doped Carbon Quantum Dots in Phenazine and Quinoxaline Sensitized Solar Cells, *Electrochim. Acta*, 2024, 144580.
- 22 W. Ling, F. Wu, W. Yuan, L. Zhu, Q. Li and Z. Li, Hole-Transporting Materials with Rational Combination of Pyridine and Dibenzo [a, c] phenazine as Electron Acceptor for Dopant-Free Perovskite Solar Cells, *Chin. J. Chem.*, 2024, **42**(10), 1100–1106.



23 S. Khanam, S. J. Akram, R. A. Khera, S. T. Zohra, A. M. Shawky, N. S. Alatawi, M. A. Ibrahim and E. U. Rashid, Exploration of charge transfer analysis and photovoltaics properties of ADA type non-fullerene phenazine based molecules to enhance the organic solar cell properties, *J. Mol. Graph. Model.*, 2023, **125**, 108580.

24 X. Li, R. Peng, Y. Qiu, Y. Zhang, J. Shi, S. Gao, H. Liu, F. Jin and Z. Ge, Selenization Strategy of Phenazine-based Non-Fullerene Acceptors Promotes Photon Harvesting and Reduces Voltage Loss in Organic Solar Cells, *Adv. Funct. Mater.*, 2025, **35**(3), 2413259.

25 T. Wang, W. Li, J. Xu, C. Hu, W. Luo, X. Zhao, Y. Hu and Z. Yuan, Phenazine-based non-fused electron acceptors for high-performance organic solar cells, *J. Mater. Chem. C*, 2025, **13**, 5591–5598.

26 F.-M. Xie, H.-Z. Li, G.-L. Dai, Y.-Q. Li, T. Cheng, M. Xie, J.-X. Tang and X. Zhao, Rational molecular design of dibenzo [a, c] phenazine-based thermally activated delayed fluorescence emitters for orange-red OLEDs with EQE up to 22.0%, *ACS Appl. Mater. Interfaces*, 2019, **11**(29), 26144–26151.

27 K. Matsumoto, K. Yamashita, Y. Sakoda, H. Ezoe, Y. Tanaka, T. Okazaki, M. Ohkita, S. Tanaka, Y. Aoki and D. Kiriya, Organic Thin-film Solar Cells Using Benzotri thiophene Derivatives Bearing Acceptor Units as Non-Fullerene Acceptors, *Eur. J. Org. Chem.*, 2021, (33), 4620–4629.

28 A. Wakamiya, H. Nishimura, T. Fukushima, F. Suzuki, A. Saeki, S. Seki, I. Osaka, T. Sasamori, M. Murata and Y. Murata, On-Top π -Stacking of Quasiplanar Molecules in Hole-Transporting Materials: Inducing Anisotropic Carrier Mobility in Amorphous Films, *Angew. Chem., Int. Ed.*, 2014, **53**(23), 5800–5804.

29 X. Huang, J. Oh, Y. Cheng, B. Huang, S. Ding, Q. He, F. Wu, C. Yang, L. Chen and Y. Chen, Narrow band-gap materials with overlapping absorption simultaneously increase the open circuit voltage and average visible transmittance of semitransparent organic solar cells, *J. Mater. Chem. A*, 2021, **9**(9), 5711–5719.

30 Y. Ding, S. Lu, J. Chang, E. Feng, H. Li, C. Long, Y. Yang, C. Yi, Z. Zheng and L. Ding, The Molecular Additive N-Acetyl-L-Phenylalanine Delays the Crystallization and Suppresses the Phase Impurity for Achieving Triple-Cation Perovskite Solar Cells with Efficiency Over 25%, *Small*, 2025, **21**(3), 2410601.

31 M. Burgelman, P. Nollet and S. Degrave, Modelling polycrystalline semiconductor solar cells, *Thin Solid Films*, 2000, **361**, 527–532.

32 H. R. Abdul Ameer, A. N. Jarad, K. H. Salem, H. S. Hadi, M. A. Alkhafaji, R. S. Zabibah, K. A. Mohammed, K. Kumar Saxena, D. Buddhi and H. Singh, A role of back contact and temperature on the parameters of CdTe solar cell, *Adv. Mater. Process. Technol.*, 2024, **10**(2), 497–505.

33 J. Rumble, *CRC Handbook of Chemistry and Physics Version 2008*, CRC Press, 2008.

34 X. Xie, G. Liu, C. Xu, S. Li, Z. Liu and E.-C. Lee, Tuning the work function of indium-tin-oxide electrodes for low-temperature-processed, titanium-oxide-free perovskite solar cells, *Org. Electron.*, 2017, **44**, 120–125.

35 Y. Shen, L. Scudiero and M. C. Gupta, Temperature dependence of open-circuit voltage and UPS study for P3HT: PCBM organic solar cells, *IEEE J. Photovoltaics*, 2012, **2**(4), 512–518.

36 S. Park, J. Jeong, G. Hyun, M. Kim, H. Lee and Y. Yi, The origin of high PCE in PTB7 based photovoltaics: proper charge neutrality level and free energy of charge separation at PTB7/PC71BM interface, *Sci. Rep.*, 2016, **6**(1), 35262.

37 S. Nam, J. Seo, S. Woo, W. H. Kim, H. Kim, D. D. Bradley and Y. Kim, Inverted polymer fullerene solar cells exceeding 10% efficiency with poly (2-ethyl-2-oxazoline) nanodots on electron-collecting buffer layers, *Nat. Commun.*, 2015, **6**(1), 8929.

38 A. K. Sharma, N. K. Chourasia, P. K. Jha, R. Kumar, M. Kumar and R. K. Chourasia, Characteristic features and performance investigations of a PTB7: PC71BM/PFN: Br pure organic solar cell using SCAPS-1D, *J. Electron. Mater.*, 2023, **52**(7), 4302–4311.

39 T. Li, K. Wang, G. Cai, Y. Li, H. Liu, Y. Jia, Z. Zhang, X. Lu, Y. Yang and Y. Lin, Asymmetric glycolated substitution for enhanced permittivity and ecocompatibility of high-performance photovoltaic electron acceptor, *JACS Au*, 2021, **1**(10), 1733–1742.

40 B. Ebenhoch, S. A. Thomson, K. Genevičius, G. Juška and I. D. Samuel, Charge carrier mobility of the organic photovoltaic materials PTB7 and PC71BM and its influence on device performance, *Org. Electron.*, 2015, **22**, 62–68.

41 J. Fu, Q. Yang, P. Huang, S. Chung, K. Cho, Z. Kan, H. Liu, X. Lu, Y. Lang and H. Lai, Rational molecular and device design enables organic solar cells approaching 20% efficiency, *Nat. Commun.*, 2024, **15**(1), 1830.

42 M. Nofil, E. Raza, F. Aziz, A. Supangat and N. Abbas, Optimizing small molecule-based organic solar cells with metal phthalocyanines for enhanced efficiency and stability, *Inorg. Chem. Commun.*, 2025, **173**, 113812.

43 M. J. Cho, J. Seo, K. H. Kim, D. H. Choi and P. N. Prasad, Enhanced Performance of Organic Photovoltaic Cells Fabricated with a Methyl Thiophene-3-Carboxylate-Containing Alternating Conjugated Copolymer, *Macromol. Rapid Commun.*, 2012, **33**(2), 146–151.

44 W. Abdelaziz, A. Zekry, A. Shaker and M. Abouelatta, Numerical study of organic graded bulk heterojunction solar cell using SCAPS simulation, *Sol. Energy*, 2020, **211**, 375–382.

45 U. K. Prajapati, E. Soni, M. Solanki and J. Rani, Enhancing the efficiency of PM6:Y6 bulk-heterojunction organic solar cells through SCAPS simulation optimization, *Chin. J. Phys.*, 2024, **92**, 1414–1425.

46 M. K. Mohammed, Boosting Efficiency in Carbon Nanotube-Integrated Perovskite Photovoltaics, *Langmuir*, 2024, **40**(51), 27114–27125.

47 M. A. Nalianya, C. Awino, H. Barasa, V. Odari, F. Gaitho, B. Omogo and M. Mageto, Numerical study of lead free CsSn0. 5Ge0. 5I3 perovskite solar cell by SCAPS-1D, *Optik*, 2021, **248**, 168060.



48 H. Benali, B. Hartiti, F. Lmai, A. Batan, S. Fadili and P. Thevenin, Enhancing the efficiency of the organic-inorganic hybrid perovskite cells using Al-doped ZnO as an Electron Transport Layer and CNTs as a Hole Transport Layer: an experimental and numerical study, *Optik*, 2024, **304**, 171733.

49 R. Singh, S. Sandhu and J.-J. Lee, Elucidating the effect of shunt losses on the performance of mesoporous perovskite solar cells, *Sol. Energy*, 2019, **193**, 956–961.

50 M. Hu, H. Xu, H. Deng, Y. Wang, T. Yang, Z. Zhang and J. Li, L-Arginine-Doped PFN-Br as a Cathode Interlayer for Conventional Organic Solar Cells, *Energy Technol.*, 2024, **12**(6), 2301447.

51 R. Ranjan, N. Anand, M. N. Tripathi, N. Srivastava, A. K. Sharma, M. Yoshimura, L. Chang and R. N. Tiwari, SCAPS study on the effect of various hole transport layer on highly efficient 31.86% eco-friendly CZTS based solar cell, *Sci. Rep.*, 2023, **13**(1), 18411.

52 Y. He, L. Xu, C. Yang, X. Guo and S. Li, Design and numerical investigation of a lead-free inorganic layered double perovskite $\text{Cs}_4\text{CuSb}_2\text{Cl}_{12}$ nanocrystal solar cell by SCAPS-1D, *Nanomaterials*, 2021, **11**(9), 2321.

53 Y. Huo, J. Zhu, X.-Z. Wang, C. Yan, Y.-F. Chai, Z.-Z. Chen, X. Zhan and H.-L. Zhang, Small molecule donors based on benzodithiophene and diketopyrrolopyrrole compatible with both fullerene and non-fullerene acceptors, *J. Mater. Chem. C*, 2018, **6**(22), 5843–5848.

54 Y. Lin, J. Wang, T. Li, Y. Wu, C. Wang, L. Han, Y. Yao, W. Ma and X. Zhan, Efficient fullerene-free organic solar cells based on fused-ring oligomer molecules, *J. Mater. Chem. A*, 2016, **4**(4), 1486–1494.

55 D. Yang, Y. Wang, T. Sano, F. Gao, H. Sasabe and J. Kido, A minimal non-radiative recombination loss for efficient non-fullerene all-small-molecule organic solar cells with a low energy loss of 0.54 eV and high open-circuit voltage of 1.15 V, *J. Mater. Chem. A*, 2018, **6**(28), 13918–13924.

56 Z. Zhang, J. Miao, Z. Ding, B. Kan, B. Lin, X. Wan, W. Ma, Y. Chen, X. Long and C. Dou, Efficient and thermally stable organic solar cells based on small molecule donor and polymer acceptor, *Nat. Commun.*, 2019, **10**(1), 3271.

57 H. Bin, Y. Yang, Z.-G. Zhang, L. Ye, M. Ghasemi, S. Chen, Y. Zhang, C. Zhang, C. Sun and L. Xue, 9.73% efficiency nonfullerene all organic small molecule solar cells with absorption-complementary donor and acceptor, *J. Am. Chem. Soc.*, 2017, **139**(14), 5085–5094.

58 J. Guo, H. Bin, W. Wang, B. Chen, J. Guo, R. Sun, Z.-G. Zhang, X. Jiao, Y. Li and J. Min, All-small molecule solar cells based on donor molecule optimization with highly enhanced efficiency and stability, *J. Mater. Chem. A*, 2018, **6**(32), 15675–15683.

59 L. Yang, S. Zhang, C. He, J. Zhang, Y. Yang, J. Zhu, Y. Cui, W. Zhao, H. Zhang and Y. Zhang, Modulating molecular orientation enables efficient nonfullerene small-molecule organic solar cells, *Chem. Mater.*, 2018, **30**(6), 2129–2134.

60 K. Gao, S. B. Jo, X. Shi, L. Nian, M. Zhang, Y. Kan, F. Lin, B. Kan, B. Xu and Q. Rong, Over 12% efficiency nonfullerene all-small-molecule organic solar cells with sequentially evolved multilength scale morphologies, *Adv. Mater.*, 2019, **31**(12), 1807842.

61 W. Gao, R. Ma, T. A. Dela Peña, C. Yan, H. Li, M. Li, J. Wu, P. Cheng, C. Zhong and Z. Wei, Efficient all-small-molecule organic solar cells processed with non-halogen solvent, *Nat. Commun.*, 2024, **15**(1), 1946.

62 J. Guo, B. Qiu, D. Yang, C. Zhu, L. Zhou, C. Su, U. S. Jeng, X. Xia, X. Lu and L. Meng, 15.71% Efficiency all-small-molecule organic solar cells based on low-cost synthesized donor molecules, *Adv. Funct. Mater.*, 2022, **32**(13), 2110159.

63 S. Wang, L.-Y. Xu, B. Xiao, M. Chen, M. Zhang, W. Gao, B. Xiao, A. K.-Y. Jen, R. Yang and J. Min, Designing dithieno-benzodithiophene-based small molecule donors for thickness-tolerant and large-scale polymer solar cells, *Energy Environ. Sci.*, 2024, **17**(7), 2610–2620.